Plasma Chem Plasma Process (2013) 33:479–490
DOI 10.1007/s11090-013-9441-0

ORIGINAL PAPER

Designing Atmospheric-Pressure Plasma Sources for Surface Engineering of Nanomaterials

Wei Yan · Zhao Jun Han · Wen Zheng Liu · Xin Pei Lu · B. Toan Phung · Kostya Ostrikov

Received: 6 December 2012 / Accepted: 18 January 2013 / Published online: 2 February 2013

Abstract Atmospheric-pressure plasma processing techniques emerge as efficient and convenient tools to engineer a variety of nanomaterials for advanced applications in nanoscience and nanotechnology. This work presents different methods, including using a quasi-sinusoidal high-voltage generator, a radio-frequency power supply, and a uni-polar pulse generator, to generate atmospheric-pressure plasmas in the jet or dielectric barrier discharge configurations. The applicability of the atmospheric-pressure plasma is exemplified by the surface modification of nanoparticles for polymeric nanocomposites. Dielectric measurements reveal that representative nanocomposites with plasma modified nanoparticles exhibit notably higher dielectric breakdown strength and a significantly extended lifetime.

Keywords Atmospheric-pressure plasma · Dielectric barrier discharge · Plasma jet · Polymeric nanocomposites · Dielectric property

W. Yan · B. Toan Phung
School of Electrical Engineering and Telecommunications, The University of New South Wales, Sydney, NSW 2052, Australia

W. Yan · Z. J. Han · K. Ostrikov (✉)
Plasma Nanoscience Centre Australia (PNCA), CSIRO Materials Science and Engineering, Lindfield, NSW 2070, Australia
e-mail: kostya.ostrikov@csiro.au

W. Z. Liu
School of Electrical Engineering, Beijing Jiaotong University, Beijing 100044, People's Republic of China

X. P. Lu · K. Ostrikov
State Key Laboratory of Advanced Electromagnetic Engineering and Technology, Huazhong University of Science and Technology, Wuhan, Hubei 430074, People's Republic of China

K. Ostrikov
Complex Systems@School of Physics, The University of Sydney, Sydney, NSW 2006, Australia

Introduction

Plasmas have been widely utilized as a versatile tool in applications ranging from surface cleaning, surface activation, thin-film coatings, polymerization, to nanofabrication, biomedicine, and water purification [1–11]. As compared to the conventional chemical, mechanical and thermal routes [12], plasma-based processes are energy-efficient, environment-friendly, and easily accessible. In recent years, significant research efforts have been directed to the development of the atmospheric-pressure plasmas (APPs) [13–16]. The successful implementation of a variety of APPs has not only led to the convenient access to plasmas without the expensive vacuum systems, but also emerging applications where low-temperature and microscale plasma confinements are the main requirements [17–19].

On the other hand, functional nanomaterials have a strong potential to enable a range of novel applications that are critical for a sustainable future. The physical and chemical properties of these nanomaterials depend on structural parameters such as size, shape, dimensionality, and surface chemical bonds, and are thus very sensitive to the preparation method [20]. Unfortunately, it is not always easy and straightforward to control these parameters during the synthesis process. The development of efficient post-synthesis methods to further tailor the properties of nanomaterials thus becomes essential [21, 22]. Owing to their unique and advantageous features, APPs have a strong potential for engineering a wide range of nanomaterials in nanotechnology-enhanced products.

Traditional studies of using APPs for surface modification indicated that the plasma effects arose mainly from the interactions between the reactive species generated in the plasma (e.g., ions, electrons, and radicals) and the substrate [23, 24]. Tailoring the plasma properties by custom-designing APP reactors could thus offer a promise to selectively modify surface properties of different nanomaterials. In the present work we develop a set of practical methodologies for generating atmospheric/sub-atmospheric-pressure plasmas, including using a 30 kHz quasi-sinusoidal high-voltage (HV) generator, a 350 kHz radio-frequency (RF) power supply, and a 30 kHz uni-polar pulse generator. Two representative configurations associated with these generators are implemented, i.e., the jet configuration and the dielectric barrier discharge (DBD) configuration. These plasmas are then utilized to modify silica nanoparticles for polymer nanocomposites. We demonstrate that the APPs are effective in altering the surface properties of silica nanoparticles, which subsequently improve the dielectric performance when blended with HV insulating polymeric materials.

Experimental

High-Voltage Quasi-Sinusoidal Mode

Figure 1a shows the circuit design of the HV quasi-sinusoidal power supply, which consists of an AC/DC rectifier, a half-bridge inverter and a high-voltage step-up transformer. Specifically, a maximum 220 V AC voltage was fed into the rectifier, enabling the DC bus voltage of the rectifier to be adjustable from 0 to 310 V. The inverter operated at a switching frequency varied from 10 to 100 kHz. The two terminals of the inverter, U_a and U_b, were then connected to the primary side of the step-up transformer. Consequently, a HV output with the quasi-sinusoidal waveform could be obtained at the secondary coil of the transformer, which was then used to generate APPs.

In the actual circuit we used MOSFETs as switches for the high-frequency inverter. These MOSFETs were driven by a square wave gate signal with the adjustable pulse width.

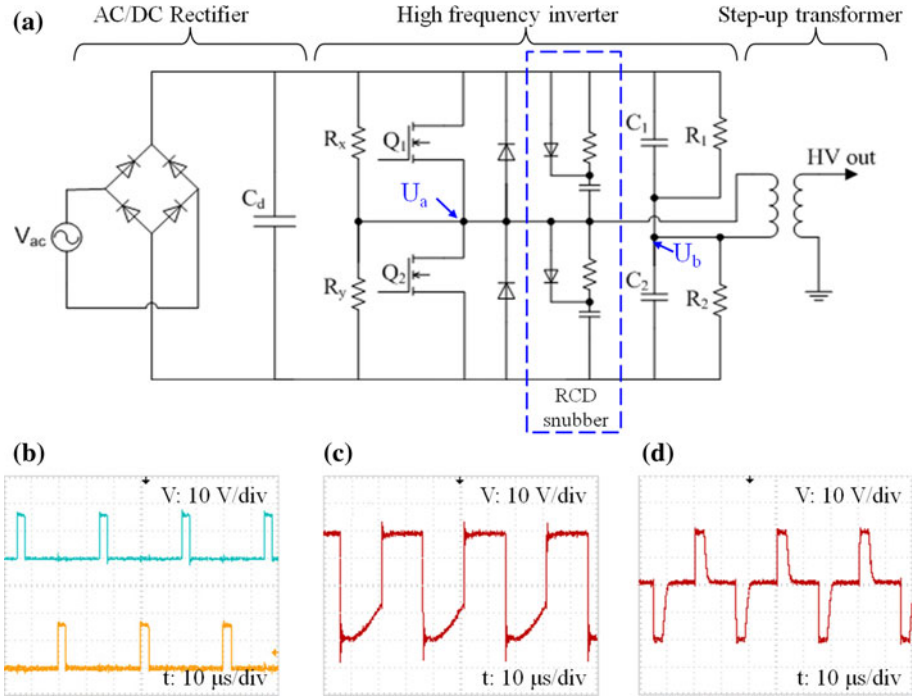

Fig. 1 **a** Circuit of high-voltage high-frequency power supply; **b** waveforms of the gate signals for MOSFETs with 180° phase difference; inverter output wavesform generated by the circuit **c** without and **d** with R_x and R_y. The dead-zone is not generated in **c**

The gate signals for the two switches had a 180° phase difference so as to set ON and OFF states alternatively, as shown in Fig. 1b. By changing the gate pulse width, the dead-zone time can be set from 0 to 90 % of the half-cycle. This dead-zone time is an important parameter to enable the effective control of the energy delivered to the plasma [25]. The inverter also consisted of two resistors, R_x and R_y as indicated in Fig. 1a, to provide charging paths for the equivalent drain-to-source capacitor of each MOSFET. The significance of using these resistors is demonstrated in Fig. 1c, d, which show that the dead-zone time was missing in the absence of R_x and R_y. It was noted that a lower value of these resistors could be beneficial for a steeper falling edge and a longer dead-zone time. However, a lower resistance was accompanied with a higher current leakage at the DC side of the rectifier. A compromise was reached by choosing 500 Ω power resistors for both R_x and R_y in the design. We also connected a Resistor–Capacitor–Diode (RCD) snubber network in parallel with each MOSFET switch to avoid over-shooting caused by the high parasitic inductance of the plasma. Finally, two identical resistors R_1 and R_2 were employed to provide a stable neutral potential (U_b) at the primary side of the transformer.

The step-up transformer was custom-made with Mn-Zn ferrite as the core material. To meet the specific requirement of the plasma generation at high frequencies, the primary winding was wound around two parallel legs of a rectangular core, while the secondary winding was wound outside of a polytetrafluoroethylene (PTFE) insulation tube covering the primary winding. This configuration enables sufficient insulation strength with small inductive leakage, which is crucial in high-frequency circuits. The step-up ratio of the transformer was 1:80 and the maximum output voltage was 30 kV peak-to-peak.

Radio-Frequency (RF) Mode

The second method we used to generate the APPs was by designing a RF power supply. The circuit of the RF power supply is shown in Fig. 2. In this mode, the circuit consisted of a commercial 350 kHz RF generator unit with a built-in matching network (PDX 500, Advanced Energy) and a customized RF step-up transformer (AL-T500-V200, Amp-Line Corporation). A resistor was also used to limit the current and possibly stabilize the plasmas generated in either jet or DBD configuration.

High-Frequency Uni-Polar Pulses

The third type of APPs was generated by uni-polar HV pulses at high repetition rates. The practical circuit is depicted in Fig. 3, where the HV pulses were produced by connecting an AC supply, a step-up transformer, a diode converter bridge, a DC buffer, and four insulated-gate bipolar transistors (IGBTs) in series. The IGBTs were triggered by synchronized and electrically isolated gate signals. Voltage balancing resistors were also connected in parallel with each of the switch modules to distribute the voltage evenly. In addition, snubber circuits were included to prevent voltage over-shooting. The fast switching of the IGBTs could lead to a high rate of current change (dI/dt) up to 20 kA/s.

Preparation of Polymer Nanocomposites

To demonstrate the applicability of APPs, we fabricated polymer nanocomposites with plasma modified nanoparticles. In brief, the epoxy resin (RX771C/NC) containing bisphenol-A diglycidyl ether (BADGE) was obtained from ROBNOR RESINS Ltd. The curing agent (ARADUR HY 1300 GB) consisted of triethylenetetramine (TETA) was supplied by Huntsman Advanced Materials. This thermoset epoxy resin had been widely

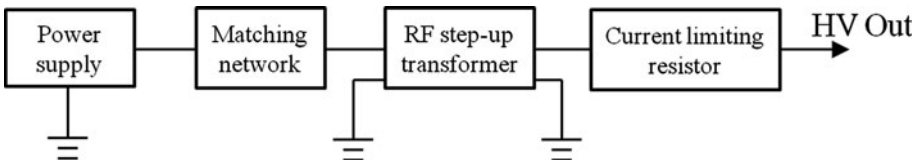

Fig. 2 Circuit diagram of the radio-frequency power supply

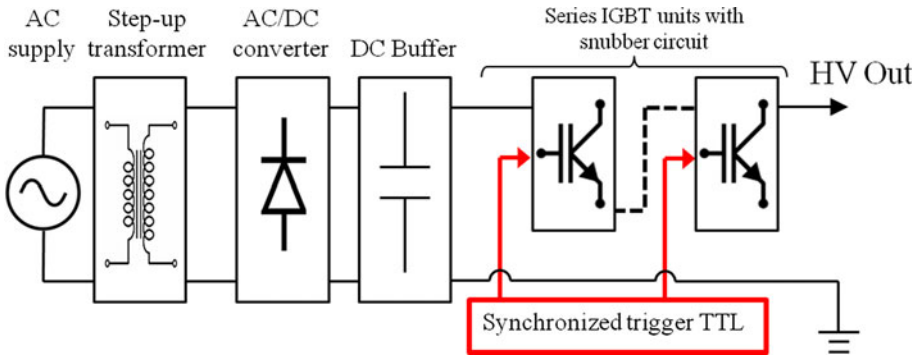

Fig. 3 Circuit design of the high-frequency uni-polar pulses power supply

used as insulation materials in high-voltage applications [26]. Amorphous silicon dioxide (SiO_2) nanoparticles with an average size of 16 nm and a surface area of 110 m^2/g were supplied from EVONIK Industries (Aerosil R972). The as-received SiO_2 nanoparticles were coated with dimethyldichlorosilane (DDS), giving rise to silane functional groups on the surface. Both untreated and plasma-treated nanoparticles were mixed with the epoxy resin at 3 wt% and the nanocomposites were denoted as UTNC and PTNC, respectively.

Characterization Techniques

The type of species generated in the APPs was identified using optical emission spectroscope (OES) which can scan the wavelength from 200 to 1,100 nm. The surface chemistry of pristine and plasma-treated nanoparticles was investigated using Fourier transform infra-red (FTIR) spectroscopy. The morphology of the polymer nanocomposites was obtained by field-emission scanning electron microscope (FESEM). To mitigate the surface charging effect, all samples were coated with a thin Au layer (less than 10 nm) prior to the SEM imaging. In addition, the dielectric constant of polymer nanocomposites was obtained by electrical impedance spectroscopy (EIS) scanning from 0.1 Hz to 1 MHz. The dielectric breakdown strength measurement was carried out on thin sample sheets with a rod-to-plane electrode configuration according to the ASTM Standard 149. Alternating current (AC) applied to the rod electrode was ramped from 0 V until the sample was broken down. For each material, 20 times of breakdown were performed. On the other hand, the endurance test was carried out using a needle-to-plane electrode configuration. The gap between the needle and the planar ground electrode was 2 mm. An AC voltage of 7.5 kV (rms) at a frequency of 300 Hz was applied to the needle electrode. The breakdown time was then recorded for each sample.

Results and Discussion

Generation of Atmospheric-Pressure Plasmas

First, we used the HV quasi-sinusoidal power supply (Fig. 1a) to generate atmospheric/sub-atmospheric-pressure plasmas in a parallel-plate DBD configuration, where the electrodes had a diameter of 60 mm. Air was used as the working gas and the pressure was gradually increased from 0.1 to 1.0 atm. As an example, Fig. 4a shows the plasma generated in a closed chamber at 33 kHz with 10 % gate pulse width and Fig. 4b shows the corresponding current waveforms at different pressures. One can see from these figures that the plasma confinement has improved at higher pressures. At around 0.7 atm, unstable streamers started to appear near the electrode (shown as multiple current peaks in Fig. 4b) [27]. It is known that these streamers contain high-energy electrons which are likely to induce over-heating on the substrates to be treated [28]. Such effect should therefore be avoided if low-temperature processes are desired.

The HV power supply was also implemented to generate plasmas in a jet configuration. Relevant studies associated with the design of this configuration could be found elsewhere [29]. Here we used a quartz nozzle with an inner tungsten wire electrode. The diameters of the nozzle and the wire electrode were 3 and 1 mm, respectively. Another metal wire wrapped around the nozzle was used as the ground electrode. A helium gas flow at 2.26 L/min was used to enable the plasma to emit from the nozzle when the rod electrode was powered. Figure 4c shows the plasmas generated at different applied voltages. It can be seen that the maximum length of the uniform plasma plume was obtained at $\sim$3 kV.

Next, we employed the RF power supply (Fig. 2) to generate the APPs in both DBD and jet configurations. Figure 5a shows the plasmas generated in a DBD configuration. As elaborated in the next section, this setup has been used to treat SiO_2 nanoparticles to obtain a uniform dispersion of nanoparticles in the HV insulation polymers. Because of the large volume of the plasma, about 50 mg SiO_2 nanoparticles could be effectively treated simultaneously.

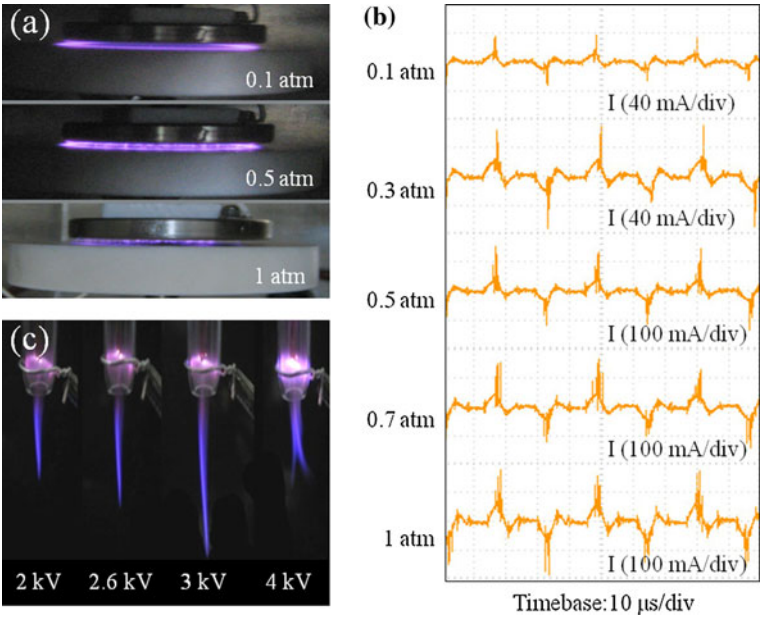

Fig. 4 **a** Plasmas generated by the HV quasi-sinusoidal power supply at different pressures using the parallel-plate DBD configuration; **b** current waveforms of the DBD plasmas at the inception voltages of different pressures; **c** the atmospheric-pressure plasma jets operated at different voltages. The longest plasma plume was obtained at 3 kV rms voltage

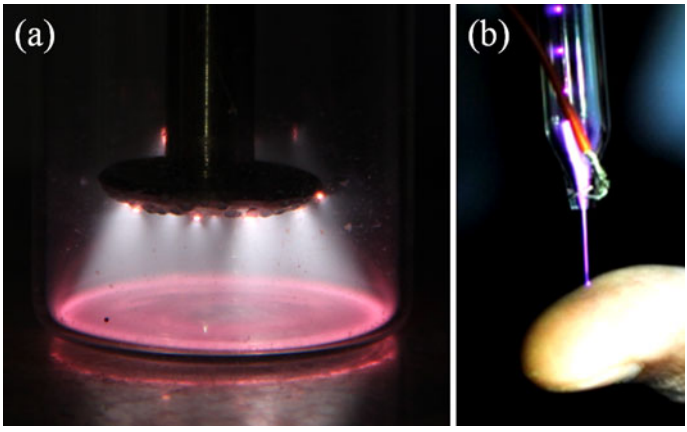

Fig. 5 RF plasmas generated in **a** the DBD and **b** the jet mode. The plasma plume in **b** is at a low temperature condition which can be safely touched by a human finger

Figure 5b shows the atmospheric plasma operated in the RF jet mode. The diameters of the nozzle and the wire electrode were both 1 mm. The helium gas flow was 0.8 L/min. In this case, a more focused (less than 100 μm in diameter) plasma plume was observed as compared to the one generated by the high-frequency quasi-sinusoidal power supply (see Fig. 4c). This plasma jet source is particularly useful for the localised surface modification of nanomaterials without causing any significant thermal damages [29–32].

We also investigated the reactive species generated in the APPs. Figure 6 compares the OES spectra of the RF plasmas generated in the DBD and jet configurations. Helium peaks at 588, 668, 707, and 728 nm can be found in both spectra. O (777 nm), H (656 nm), N_2 (365 and 428 nm), N_2^+ (390 nm), NH (336 nm), and OH (307 nm) were also detected due to the presence of N_2, H_2O, and O_2 species in APPs [33]. However, it was noted that the magnitude of the hydroxyl radicals (OH) was much higher in the DBD than in the jet plasma. These highly-reactive OH species may be used for a variety of surface modifications of the nanoparticles, as detailed in the next section [34, 35].

Finally, the uni-polar HV pulses (Fig. 3) were applied to the parallel-plate DBD electrodes with the same configuration as shown in Fig. 4a. In this case, however, the discharge could only be operated at 0.1 atm when air was used as the working gas. Figure 7a shows the uniformly diffused plasma ignited within the electrode gap. The intensity of the plasma could be controlled by tuning the pulse width, as demonstrated in Fig. 7b, c. It was found that increasing the voltage pulse width from 10 to 30 % significantly reduced the magnitude of the discharging current.

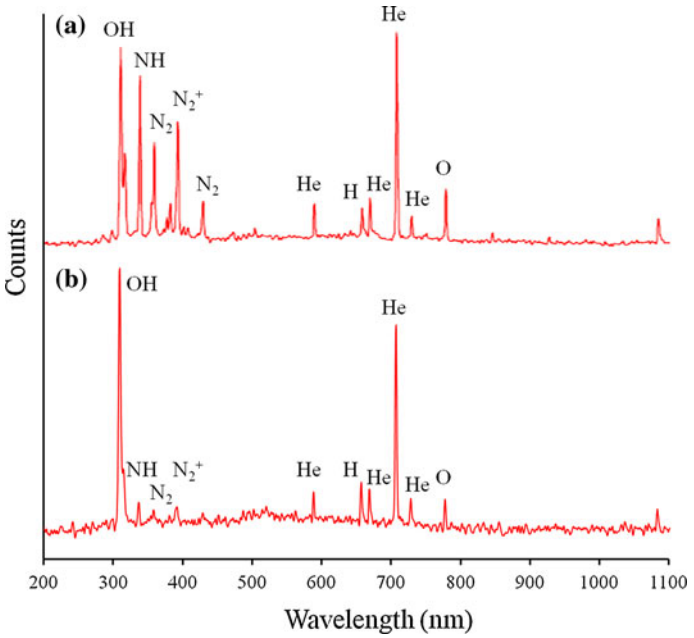

Fig. 6 The optical emission spectra of the RF plasma operated in **a** the jet and **b** the DBD configurations

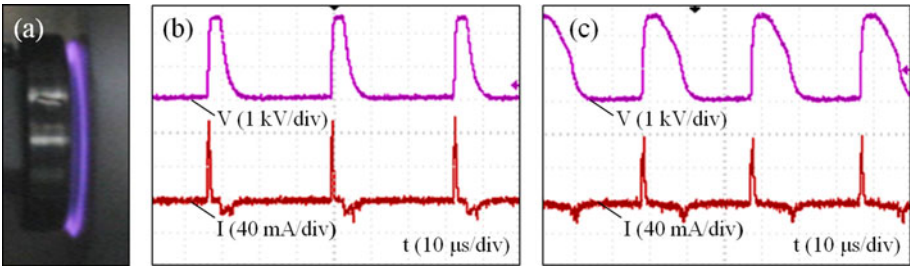

Fig. 7 **a** The DBD plasma generated by the uni-polar HV pulsar at 0.1 atm; **b** and **c** show the voltage and current waveforms of the plasma generated with 10 and 30 % pulse width, respectively

Fabrication of Polymeric Nanocomposite Dielectrics

An important application of APPs is in the fabrication of polymer nanocomposites. These nanocomposites comprise inorganic nanoparticles embedded into a polymeric matrix [36, 37]. In recent years, various nanoparticles including $BaTiO_3$, $SrTiO_3$, SiO_2, TiO_2 or Al_2O_3 have been blended with polymers to tailor the dielectric constant, alter space charge distribution, and enhance electrical tolerance for next-generation high-voltage insulation systems and installations [38–40]. It is known that the properties and performance of the nanocomposites are highly-sensitive to the dispersion uniformity of the nanoparticles and the interfacial interactions between the fillers and the polymer matrices. Unfortunately, the nanoparticles of our interest are typically inorganic, which may lead to unwanted agglomeration in the organic polymeric matrices [41].

The reactive species generated in APPs can effectively modify the surface energy of nanoparticles at room temperature [42]. In addition, plasma-surface reactions such as ion bombardment, electron collisions, and photon interactions can also increase the reactivity of the nanoparticles by breaking surface chemical bonds thereby creating free radicals. These effects may lead to improved dispersion uniformity and stronger interaction with the surrounding polymer molecules when the polymer and the nanoparticles are mixed. Because of the large plasma volume and the high concentration of OH species, we utilized the RF plasma in DBD mode to treat the SiO_2 nanoparticles. The power density of the plasma volume was estimated to be 60 mW/cm^3, a typical value for cold plasma processing [43]. 50 mg of SiO_2 nanoparticles were exposed to the plasma for 20 min. A gas outlet blew through a water bottle to prevent nanoparticles from escaping to the atmosphere [44]. The temperature of the plasma in the reactor was kept below 80 °C. During this process, mechanical stirring was performed to ensure a uniform exposure. After the plasma treatment, the nanoparticles and the curing agent were added into the epoxy resin to synthesize the nanocomposites.

The surface chemistry of nanoparticles was investigated using FTIR. As shown in Fig. 8, two sharp peaks at 1,070 cm^{-1} (Si–O–Si stretching) and 806 cm^{-1} (Si–O bending) could be observed for the pure SiO_2 nanoparticles. On the other hand, three additional peaks were found around 870, 840, and 760 cm^{-1} for the as-received (silane-coated) SiO_2 nanoparticles, corresponding to the Si–O–Si bridges, the $–OSiCH_3$ groups, and the $–Si(CH_3)_3$ groups, respectively [45]. After the plasma treatment, both peaks around 840 and 760 cm^{-1} were reduced. This was a clear indication that the surface Si–C bonds were broken and free radicals may have formed. As a result, the surface reactivity of the

nanoparticles could be increased, leading to the formation of stronger chemical bonds when mixed with the polymer matrices [40]. Indeed, the cross-sectional scanning electron microscopy (SEM) images indicated that the nanoparticles were dispersed more evenly in the plasma-modified (i.e., PTNC) than in the unmodified (i.e., UTNC) samples, as shown in Fig. 9a, b, respectively. High-resolution SEM images further revealed that the as-received SiO_2 nanoparticles may form aggregates in the polymer matrix with a size much larger than that of the modified nanoparticles (the insets in Fig. 9a, b).

Figure 10 shows the dielectric constant (k) of the UTNC and PTNC samples as a function of the frequency. It is found that the PTNC had a lower k than that of UTNC at the high frequency region (100 Hz–1 MHz); whereas an opposite was observed at the low frequency region (0.1–0.5 Hz). According to *Nelson* et al. [36], the reduced k values of the nanocomposites could be attributed to the restriction on the mobility of polymer molecules imposed by the nanoparticles. In a similar way, we speculated that the Si–N bonds formed between the functional surface groups of SiO_2 nanoparticles (Fig. 8) and the epoxy resin polymer may impair the dipole moments of the polymer chain [40]; consequently, the dielectric constant was reduced. At low frequencies, however, this effect can be weakened by the electrical double-layer around the nanoparticles. It was shown that charge carriers in the double-layer can be transferred through the interfacial region, which may lead to an

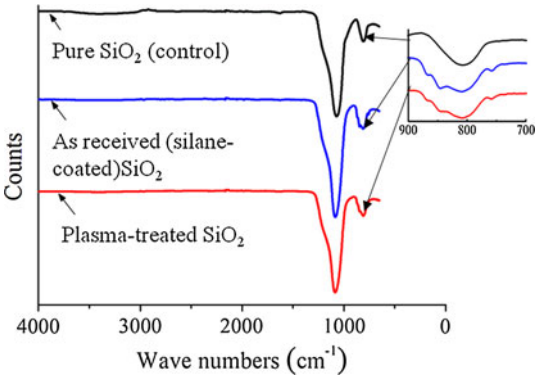

Fig. 8 FTIR spectra of the uncoated, the as-received (saline-coated), and the plasma-treated SiO_2 nanoparticles

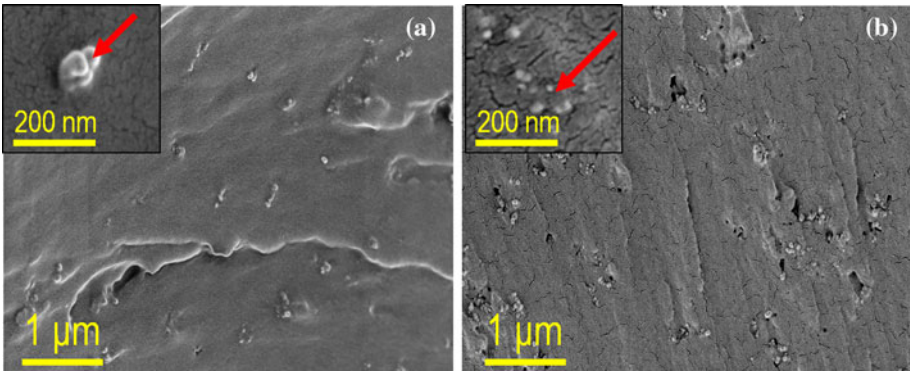

Fig. 9 SEM images of the nanocomposites with **a** the as-received and **b** the plasma-treated SiO_2 nanoparticles. *Arrows in the insets* point to the embedded nanoparticles

induced polarization around the nanoparticles and hence an increased k value at low frequencies [46, 47].

We then conducted the dielectric breakdown and endurance tests to evaluate the insulation properties of the synthesized organic–inorganic nanocomposites. The schematic of the dielectric breakdown test is shown in Fig. 11a. Figure 11b shows that the inclusion of the as-received nanoparticles (i.e., the UTNC sample) had increased the breakdown strength from 53 kV/mm of the pristine epoxy resin (i.e., the PER sample) to 116 kV/mm. The nanocomposites with the plasma-treated nanoparticles (i.e., the PTNC sample) further improved the breakdown strength by another 23.3 % to 143 kV/mm.

The experimental set-up of endurance test is sketched in Fig. 11c. It was observed that electrical breakdown occurred when the electrical trees had propagated from the needle tip

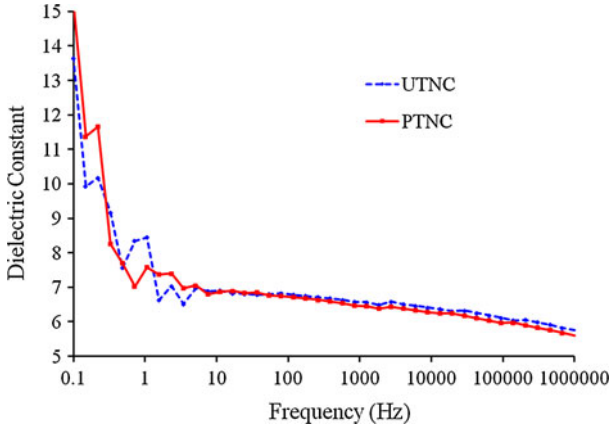

Fig. 10 Dielectric constant of the UTNC and PTNC nanocomposites at frequencies from 0.1 Hz to 1 MHz

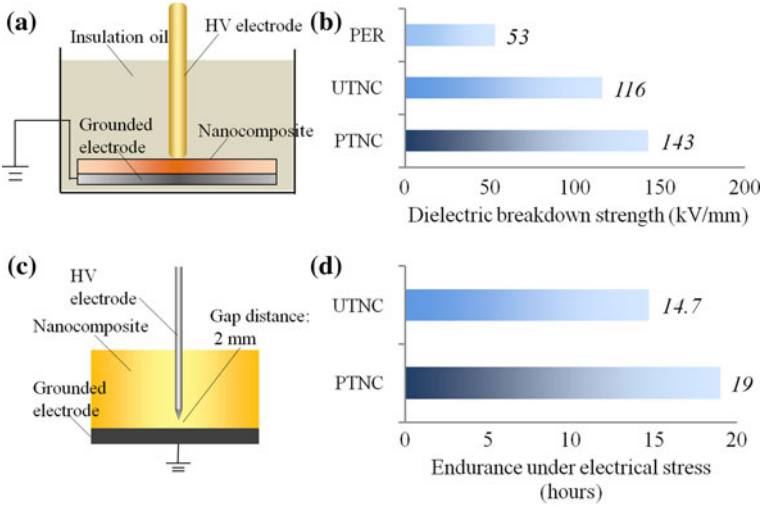

Fig. 11 **a** The rod-to-plane electrode configuration used in the electrical breakdown test; **b** the bar chart of the breakdown strength of the pure epoxy resin (PER), nanocomposite with untreated nanoparticles (UTNC), and nanocomposite with plasma-treated nanoparticles (PTNC) samples; **c** the needle-to-plane electrode used in the endurance test; **d** the bar chart of the endurance time of the UTNC and PTNC samples

to the grounded electrode [40]. The breakdown time of each sample was recorded as the endurance (lifetime) under constant electrical stress. Figure 11d indicates that the endurance of the PTNC sample had significantly increased from 14.7 h of the UTNC samples to 19 h [40].

Conclusion

Atmospheric-pressure plasmas offer an effective, economic, and environment-friendly route for engineering a broad range of functional nanomaterials. The present study has elaborated a set of practical methodologies for generating atmospheric-pressure plasmas by a customized design of various HV circuits and electrode configurations. The applicability of these plasma processing techniques has been demonstrated through the polymer nanocomposites. Our results show that polymer nanocomposites blended with plasma-treated SiO_2 nanoparticles possessed lower dielectric constant at high frequencies, much higher dielectric breakdown strength, and prolonged lifetime under high electrical stress. These findings show the possibility of future industrial process using atmospheric-pressure plasma technology and indicate its promising future in processing nanomaterials for advanced applications.

References

1. Ostrikov K (2005) Rev Mod Phys 77:489–511
2. Chen QD, Dai LM, Gao M, Huang SM, Mau A (2001) J Phys Chem B 105:618–622
3. Morent R, De Geyter N, Verschuren J, De Clerck K, Kiekens P, Leys C (2008) Surf Coat Tech 202:3427–3449
4. Deb B, Kumar V, Druffel TL, Sunkara MK (2009) Nanotechnology 20:465701
5. Choi K, Ghosh S, Lim J, Lee CM (2003) Appl Surf Sci 206:355–364
6. Moravej M, Yang X, Nowling GR, Chang JP, Hicks RF, Babayan SE (2004) J Appl Phys 96:7011–7017
7. Shi DL, Wang SX, van Ooij WJ, Wang LM, Zhao JG, Yu Z (2001) Appl Phys Lett 78:1243–1245
8. Grinevich VI, Kvitkova EY, Plastinina NA, Rybkin VV (2011) Plasma Chem Plasma Process 31:573–583
9. Cvelbar U, Ostrikov K, Mozetic M (2008) Nanotechnology 19:405605
10. Long JD, Xu S, Cai JW, Jiang N, Lu JH, Ostrikov KN, Diong CH (2002) Mater Sci Eng, C 20:175–180
11. Chen C, Ogino A, Wang X, Nagatsu M (2010) Appl Phys Lett 96:131504
12. Ramajo L, Castro MS, Reboredo MM (2007) Compos Part A 38:1852–1859
13. Mariotti D, Sankaran RM (2011) J Phys D-Appl Phys 44:174023
14. Pei X, Lu X, Liu J, Liu D, Yang Y, Ostrikov K, Chu PK, Pan Y (2012) J Phys D-Appl Phys 45:165205
15. Chu PK, Chen JY, Wang LP, Huang N (2002) Mater Sci Eng R 36:143–206
16. Huang J, Li H, Chen W, Lv G-H, Wang X-Q, Zhang G-P, Ostrikov K, Wang P-Y, Yang S-Z (2011) Appl Phys Lett 99:253701
17. Lee SW, Liang D, Gao XPA, Sankaran RM (2011) Adv Funct Mater 21:2155–2161
18. Chiang WH, Sankaran RM (2009) Nat Mater 8:882–886
19. Mukherjee N, Wavhal D, Timmons RB (2010) ACS Appl Mater Interf 2:397–407
20. Roduner E (2006) Chem Soc Rev 35:583–592
21. Jafari R, Asadollahi S, Farzaneh M (2012) Plasma Chem Plasma Process doi:10.1007/s11090-012-9413-9
22. Du C, Huang D, Li H, Xiao M, Wang K, Zhang L, Li Z, Chen T, Mo J, Gao D, Huang Y, Liu S, Yu L, Zhang C (2012) Plasma Chem Plasma Process. doi: 10.1007/s11090-012-9412-x
23. Cui NY, Brown NMD (2002) Appl Surf Sci 189:31–38
24. Morent R, De Geyter N, Verschuren J, De Clerck K, Kiekens P, Leys C (2008) Surf Coat Technol 202:3427–3449
25. Hoshi N, Matsui A (2012) Electr Eng Jpn 180:57–64

26. Thomas S, Raman S, Mohanan P, Sebastian MT (2010) Compos Part A 41:1148–1155
27. Shashurin A, Shneider MN, Keidar M (2012) Plasma Sources Sci Technol 21:034006
28. Sima WX, Peng QJ, Yang Q, Yuan T, Shi J (2012) IEEE Trans Dielect Elect Insul 19:660–670
29. Laroussi M, Akan T (2007) Plasma Process Polym 4:777–788
30. Cao Z, Walsh JL, Kong MG (2009) Appl Phys Lett 94:021501
31. Lu X, Jiang Z, Xiong Q, Tang Z, Hu X, Pan Y (2008) Appl Phys Lett 92:081502
32. Shashurin A, Keidar M, Bronnikov S, Jurjus RA, Stepp MA (2008) Appl Phys Lett 93:181501
33. Kieft IE, van der Laan EP, Stoffels E (2004) New J Phys 6:149
34. Liu ZW, Yang XF, Zhu AM, Zhao GL, Xu Y (2008) Eur Phys J D 48:365–373
35. Liu DX, Iza F, Wang XH, Kong MG, Rong MZ (2011) Appl Phys Lett 98:221501
36. Roy M, Nelson JK, MacCrone RK, Schadler LS (2007) J Mater Sci 42:3789–3799
37. Tuncer E, Sauers I, James DR, Ellis AR, Paranthaman MP, Goyal A, More KL (2007) Nanotechnology 18:325704
38. Qi L, Lee BI, Chen SH, Samuels WD, Exarhos GJ (2005) Adv Mater 17:1777–1781
39. Imai T, Sawa F, Nakano T, Ozaki T, Shimizu T, Kozako M, Tanaka T (2006) IEEE Trans Dielect Elect Insul 13:319–326
40. Yan W, Han ZJ, Phung BT, Ostrikov K (2012) ACS Appl Mater Interf 4:2637–2642
41. Roy M, Nelson JK, MacCrone RK, Schadler LS, Reed CW, Keefe R, Zenger W (2005) IEEE Trans Dielect Elect Insul 12:629–643
42. Ostrikov K, Levchenko I, Cvelbar U, Sunkara M, Mozetic M (2010) Nanoscale 2:2012–2027
43. Tsakadze ZL, Ostrikov K, Long JD, Xu S (2004) Diamond Relat Mater 13:1923–1929
44. Han ZJ, Levchenko I, Kumar S, Yajadda MMA, Yick S, Seo DH, Martin PJ, Peel S, Kuncic Z, Ostrikov K (2011) J Phys D-Appl Phys 44:174019
45. Mathias J, Wannemacher G (1988) J Colloid Interface Sci 125:61–68
46. Tanaka T, Kozako M, Fuse N, Ohki Y (2005) IEEE Trans Dielect Elect Insul 12:669–681
47. Lewis TJ (2004) IEEE Trans Dielect Elect Insul 11:739–753